High-mass loading $V_3O_7 \cdot H_2O$ nanoarray for Zn-ion battery: New synthesis and two-stage ion intercalation chemistry

Duo Chen [a,b,c], *Mengjie Lu* [a], *Boran Wang* [d], *Hongfei Cheng* [b], *Hang Yang* [a], *Dong Cai* [c,*], *Wei Han* [a,*], *Hong Jin Fan* [b,*]

[a] Key Laboratory of Physics and Technology for Advanced Batteries (Ministry of Education), College of Physics, Jilin University, Changchun 130012, P. R. China.

[b] School of Physical and Mathematical Sciences, Nanyang Technological University, Singapore 637371, Singapore.

[c] Key Laboratory of Carbon Materials of Zhejiang Province, Wenzhou University, Wenzhou 325035, P.R. China.

[d] State Key Laboratory of Inorganic Synthesis and Preparative Chemistry, College of Chemistry, Jilin University, Changchun, 130012, P.R. China.

Corresponding Author

*E-mail: caidong17@mails.jlu.edu.cn (D. Cai)

*E-mail: whan@jlu.edu.cn (W. Han)

*E-mail: fanhj@ntu.edu.sg (H.J. Fan)

Abstract

Vanadium-based materials are promising cathode materials for aqueous rechargeable zinc-ion batteries (ZIBs). However, up to now, the detailed Zn ion intercalation mechanisms are still not fully clear. In this work, we first show a new facile synthesis approach for $V_3O_7 \cdot H_2O$ nanoarray cathode with large mass loadings (1.0 - 12 mg cm^{-2}). An empirical model is proposed to assess the utilization ratio of active materials under different mass loadings. Then, through the combination of first-principles calculations and a series of ex-situ characterizations, we identify for the first time a two-step Zn^{2+} intercalation mechanism in $V_3O_7 \cdot H_2O$. The stepwise and reversible intercalation process is manifested by different diffusion energy barriers and segmented electrochemical kinetics in various discharge depths. The nanoarray binder-free electrode is also applied in pouch cells which show high capacities than state-of-the-art ZIB pouch cells. This study may provide an elucidation for the disputed Zn^{2+} intercalation chemistry of vanadium-based cathodes in ZIBs as well as a guidance to the design of high-mass-loading battery materials.

Key words: zinc-ion battery, Zn ion intercalation, $V_3O_7 \cdot H_2O$, vanadium oxides, aqueous batteries.

1. Introduction

Owing to the increasing shortage and inhomogeneous distribution of lithium resource as well as the safety concerns, it is urgent to make a transition from the conventional lithium-ion batteries (LIBs) to more sustainable and economic, and safer batteries [1-3]. As one of the emerging candidates, aqueous rechargeable zinc-ion batteries (ZIBs) have garnered enormous attention because of the advantage of intrinsic safety without risk of flame or explosion, abundancy of all device components, and convenience of battery fabrication [4-7]. From electrochemical point of view, the Zn anode has a low redox potential (-0.76 V *vs.* standard hydrogen electrode), and the two-electron transfer of Zn^{2+}/Zn during (de)intercalation reactions can potentially provide higher energy density than monovalent alkali ions (e.g. Li^+, K^+, or Na^+) [8-10]. Therefore, ZIBs have been under the spotlight and significant progress has been made in recent years [11-14]. However, the large charge/radius ratio of Zn^{2+} causes a strong electrostatic repulsion in the host materials, resulting in the impeded insertion and sluggish diffusion kinetics [15-17]. To tackle this, it is pivotal to develop appropriate cathode materials with engineered interlayer spacing and structural water as well as nanoarchitecture.

To date, many cathode materials have been explored for ZIBs, including vanadium oxides, manganese oxides, Prussian blue analogues, and organic polymers [18]. Among them, Prussian blue analogues exhibit high discharge voltage plateaus, but suffer from unsatisfactory capacity [19, 20]. Manganese oxides exhibit moderate capacity and acceptable discharge voltage, but are hampered by the inferior rate capability and unstable cycling performance because of the unwanted phase transitions [21]. Organic polymers possess high tunability and large specific capacity, but are also hindered by rapid performance deterioration during cycling due to the issues of dissolution or decomposition [22, 23]. In comparison, most vanadium oxides (e.g. $V_2O_5 \cdot nH_2O$, VO_2, V_6O_{13},

$V_5O_{12}\cdot 6H_2O$, $V_3O_7\cdot H_2O$) can deliver high capacity, excellent rate capability and robust cycling durability, and hence they are regarded as promising cathode candidates for ZIBs [24]. Among them, layered $V_3O_7\cdot H_2O$ (also denoted as $H_2V_3O_8$) can provide prominent Zn^{2+} storage performances [9]. It possesses high electric conductivity originating from the mixed valences of V(IV) and V(V), while the high average oxidation state (+4.67) can introduce more active redox sites for high Zn^{2+} storage capacity [25, 26]. Despite the large amount of literatures on vanadium-based cathodes, unfortunately, the Zn ion storage mechanism of $V_3O_7\cdot H_2O$ still remains unclear. Meanwhile, in previous studies, the synthesis of nanostructured $V_3O_7\cdot H_2O$ as feasible cathode for ZIBs requires complex process with high energy consumption and generates byproducts that cause unavoidable pollution [27-32]. Moreover, traditional synthesis techniques by CVD, hydrothermal or electrodeposition usually deliver a low mass loading of the active material (< 2 mg cm^{-2}), which could hardly meet the demand of commercial applications [33, 34]. Hence, from the aspects of both understanding the Zn-ion storage mechanism and developing a facile synthesis method for high-mass-loading cathode materials, more research is urgently needed.

In this work, we intend to systematically investigate the Zn-ion intercalation process in $V_3O_7\cdot H_2O$. For this purpose, $V_3O_7\cdot H_2O$ nanoarrays (VOHAs) are synthesized via a facile one-step recrystallization of dissolved commercial V_2O_5 from HCl solution on carbon-fiber paper (CP), which can be directly used as a binder-free electrode for ZIBs. This fabrication process requires neither high temperature nor any additional treatment and, more importantly, can obtain high loading of $V_3O_7\cdot H_2O$. As an often-neglected issue in nano battery community, the relationship between specific capacity and mass loading of active materials is discussed and the optimal mass loading is attained by fitting the mass - capacity plot. For the electrode with a mass loading of 5 mg cm^{-2}, the VOHA delivers a high capacity of 323 mAh g^{-1} at the specific current of 0.1 A g^{-1},

which can retain a value of 155 mA g^{-1} at 2 A g^{-1}. The Zn-intercalation chemistry has been thoroughly studied through comprehensive DFT calculation and systematic ex-situ characterizations, from which a new mechanism of two-step Zn^{2+} intercalation in $V_3O_7{\cdot}H_2O$ during discharging is proved for the first time. Furthermore, the inhomogeneity of the electrochemical kinetics in different discharge depths is also revealed. This work might deepen the understanding of the Zn^{2+} storage process in vanadium-based materials and further promote the competitiveness of aqueous ZIBs to LIBs.

2. Results and discussion

The $V_3O_7{\cdot}H_2O$ nano-arrays were directly grown on the carbon paper via a facile one-step sol-gel method, as illustrated in **Fig. 1**a. The commercial V_2O_5 was firstly dissolved in 1.0 M HCl and then precipitated on carbon paper as vanadium oxide hydrate after the solvent evaporation. Because of the strong oxidizing property of vanadium (+5) cations in HCl, the V_2O_5 is reduced during recrystallization and the reaction can be expressed as "$3VO_2^+ + Cl^- + 2H_2O \rightarrow V_3O_7 \cdot H_2O + 2H^+ + \frac{1}{2}Cl_2$". The mass loading (1.0 - 12.0 mg cm^{-2}) can be controlled by modulating the volume of reaction solution, thereby it can be regarded as an efficient approach to fabricate self-support vanadium oxide-based cathode. For example, inset in **Fig. 1**a displays a 21cm × 20 cm sample electrode after the reaction, on which a uniform film of $V_3O_7{\cdot}H_2O$ array is deposited. Owing to its low cost, large-scale manufacturability and high mass loading, this synthesis method might be a potential candidate for industrial developments.

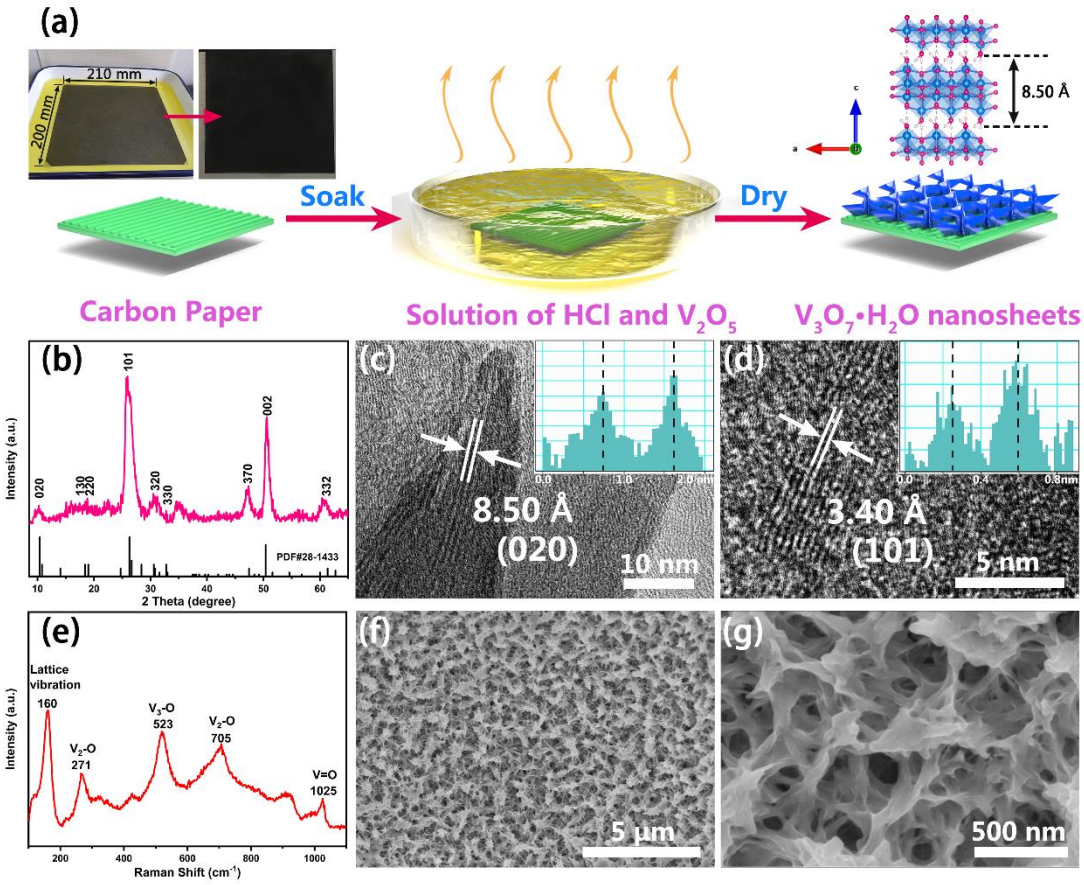

Fig. 1. Structure and morphology characterization of VOHAs. (a) Schematic of the one-step synthesis process for the binder-free VOHAs electrode. The left inset is the optical photograph of a 210mm × 200mm carbon paper soaked in the reaction solution and as-obtained VOHAs electrode, and the right one is the crystal model of $V_3O_7 \cdot H_2O$. (b) XRD pattern, (c-d) high-resolution TEM images, and (e) Raman spectrum of $V_3O_7 \cdot H_2O$ powder. (f-g) SEM images of the VOHAs with different magnifications.

The structure and morphology of the as-prepared powder collected from the reaction product was investigated using various techniques. As shown in **Fig. 1**b, the XRD pattern is in good agreement with the orthorhombic phase of $V_3O_7 \cdot H_2O$ (PDF#28-1433). The TEM images in **Fig. 1**c-d display two lattice spacings of 8.50 and 3.40 Å, which correspond to the (020) and (101)

plane of $V_3O_7 \cdot H_2O$, respectively. The layered crystal structure (Inset of **Fig. 1**a) can be considered as a favorable host framework for Zn^{2+} storage [24]. Specifically, the vanadium oxide hydrate is formed by H-bond-linked V_3O_8 layers, where the two-dimensional crystal structure in *ab*-plane is comprised of edge/corner-shared VO_6 octahedra and VO_5 square pyramids [27]. The oxygen of water is shared with a VO_5 polyhedron and the hydrogen of water forms the H-bond with the oxygen in the adjacent crystal layer. Hence the V_3O_8 layers are stacked along the *c*-axis to form the layered structure, providing the intercalation channel and host sites for Zn^{2+} [24,28]. In particular, the elastic buffer spaces between layers based on hydrogen bonding are favorable to maintaining the structural integrity and stability during the Zn^{2+} diffusion, endowing the H-bond-linked $V_3O_7 \cdot H_2O$ with superior cycling durability than other layered vanadium oxides that are held by weaker van der Waals interactions [29]. The crystal and chemical structures of orthorhombic $V_3O_7 \cdot H_2O$ were further investigated by Raman spectroscopy. As shown in **Fig. 1**e, a series of characteristic vibration peaks of $V_3O_7 \cdot H_2O$ are observed at 160, 271, 520, 705 and 1025 cm^{-1}. Specifically, the peak located at the low shift of 160 cm^{-1} originates from the lattice vibration, which is associated with the layered structure of $V_3O_7 \cdot H_2O$ [35]. The second peak at 271 cm^{-1} is attributed to the flexural mode of V_2-O [36]. The peaks located at 523 and 705 cm^{-1} are assigned to the triply (V_3-O) and doubly (V_2-O) coordinated oxygen stretching modes, corresponding to the edge- and corner-shared oxygen, respectively [37]. The Raman peak at high frequency of 1025 cm^{-1} is identified as the terminal oxygen (V=O) vibration from the unshared oxygen [25]. According to scanning electron microscope (SEM) observation, the $V_3O_7 \cdot H_2O$ array covers uniformly the substrate surface forming a cross-linked porous network (**Fig. 1**f and d). This open network structure provides unimpeded pathway for electrolyte penetration and abundant exposed

active sites, which is favorable to maintaining the capacity and rate performance of high-mass-loading electrodes.

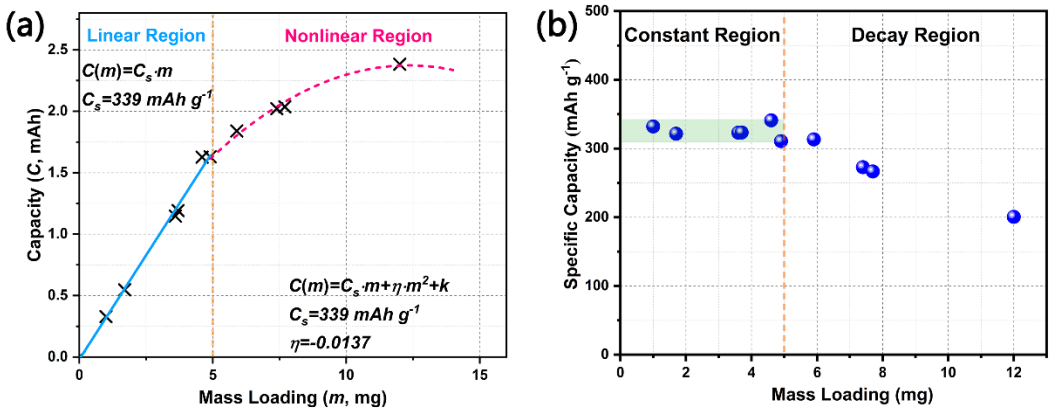

Fig. 2. Evaluation of mass loading effect. (a) The relationship between the capacity of cathode materials and mass loading. (b) The specific capacity of VOHAs at various mass loading. All of the results were collected at a specific current of 0.1 A g^{-1}.

The binder-free VOHA electrode was directly employed as the cathode, coupled with a zinc foil as the anode to fabricate the coin-type ZIB, using the aqueous electrolyte of 3 M $Zn(CF_3SO_3)_2$. Considering that the efficient manufacture method can endow the electrode with a wide range of mass loadings, we firstly intend to establish the dependence of their capacities on mass loading. The discharge capacities of a series of cathodes with different mass loading of 1.0 - 12.0 mg cm^{-2} were measured at the same current of 0.1 A g^{-1}. Their charge/discharge curves except for the sample with mass loading of 12.0 mg cm^{-2} exhibit similar shapes, which possess two pairs of obvious pseudo-platforms (**Fig. S1**). This demonstrates that the electrodes with mass loading below 12.0 mg cm^{-2} underwent similar electrochemical processes. As for the sample with the highest mass loading of 12.0 mg cm^{-2} (**Fig. S1j**), a discharge/charge platform is nearly imperceptible which might be attributed to the impeded mass transfer in the thick electrode, resulting in a relatively low capacity. To directly analyze the effect of mass loading of active

materials, the capacity versus mass loading of the cathode material is plotted (**Fig. 2a**). The fitting curve can be divided into two parts, i.e. the linear region and nonlinear region, corresponding to the fitting equations in Eq. (1) and Eq. (2), respectively.

$$C(m) = C_s m \qquad (1)$$

$$C(m) = C_s m + \eta m^2 + k \qquad (2)$$

The linear part passes through the origin and verifies that the capacity of the cathode increases proportionally with increasing mass loading. Hence, we propose that the utilization of the active materials is maximized at the end of the linear region. To show this more clearly, the specific capacity evolution at various mass loadings is plotted in **Fig. 2b**. The constant region below 5 mg cm^{-2} corresponds to the linear region, beyond which the specific capacity drops with increasing mass density. In particular, the specific capacity decays almost linearly with the increase in mass density, which is consistent with the second-order power law relationship in Eq. (2). The slop of the fitting line (C_s) corresponds to the average specific capacity, which is determined to be 339 mAh g^{-1}. The nonlinear region can be fitted by a second-order function (Eq. (2)), involving an attenuation coefficient η in the second term which could reflect the decrease in the utilization of active materials caused by the mass loading growth. Because the linear region might be considered as the circumstance without utilization decay, the maximal specific capacity (C_s) is the coefficient of the first order term in Eq. (2). Thus, we can determine the attenuation coefficient η = -0.0137 mAh mg^{-2}. A rational design of the electrode microstructure should facilitate the ion and charge transport and might effectively decrease the absolute value of attenuation coefficient under the circumstance of high mass loading. It is proposed that it is meaningful to determine the η of an electrode when the battery is evaluated for industrial production.

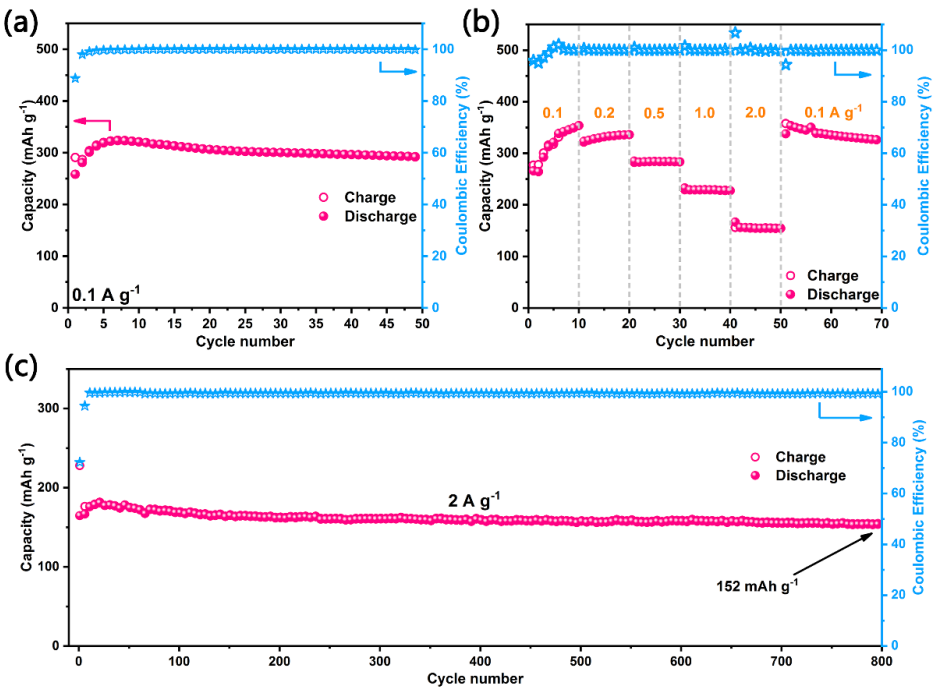

Fig. 3. Electrochemical property of ZIB. The battery is made of VOHAs cathode, Zn plate anode, and aqueous 3 M $Zn(CF_3SO_3)_2$ electrolyte. (a) Specific capacity at the current of 0.1 A g^{-1}. (b) Rate capability measured at different current densities. (c) Long-term cycling durability at 2 A g^{-1}.

Based on the above discussion, the free-standing VOHAs cathode can maintain maximal utilization with mass loading up to 5.0 mg cm^{-2}. Hence, the subsequent study was carried out to ZIB made from the 5.0-mg cm^{-2} cathode. As shown in **Fig. 3a**, the as-fabricated ZIBs could deliver a high capacity of 323 mAh g^{-1} at the current of 0.1 A g^{-1} in the initial cycles, which can retain a capacity value > 300 mAh g^{-1} after 50 cycles. It should be pointed out that the initial capacity increase might be caused by the gradual activation of the electrode to reach a stabilized interface with electrolyte. The rate capability of the VOHAs cathode is also outstanding (**Fig. 3b**), in which the average discharge capacities are 321, 331, 283, 229 and 155 mAh g^{-1} at the current densities of 0.1, 0.2, 0.5, 1.0 and 2.0 A g^{-1}, respectively. When the current returns back to 0.1 A g^{-1}, the cell can fully recover its initial capacity. Cycling durability of VOHAs electrode was further evaluated

at 2.0 A g^{-1}. As shown in **Fig. 3c**, the cell could retain 152 mAh g^{-1} after 800 cycles with slight capacity fading, indicating a reliable cycling stability. The superior specific capacity and rate capability should benefit from the abundant exposed active sites, unimpeded ion diffusion channels in the cross-linked porous nanostructure, and the rapid charge transfer from the binder-free electrode.

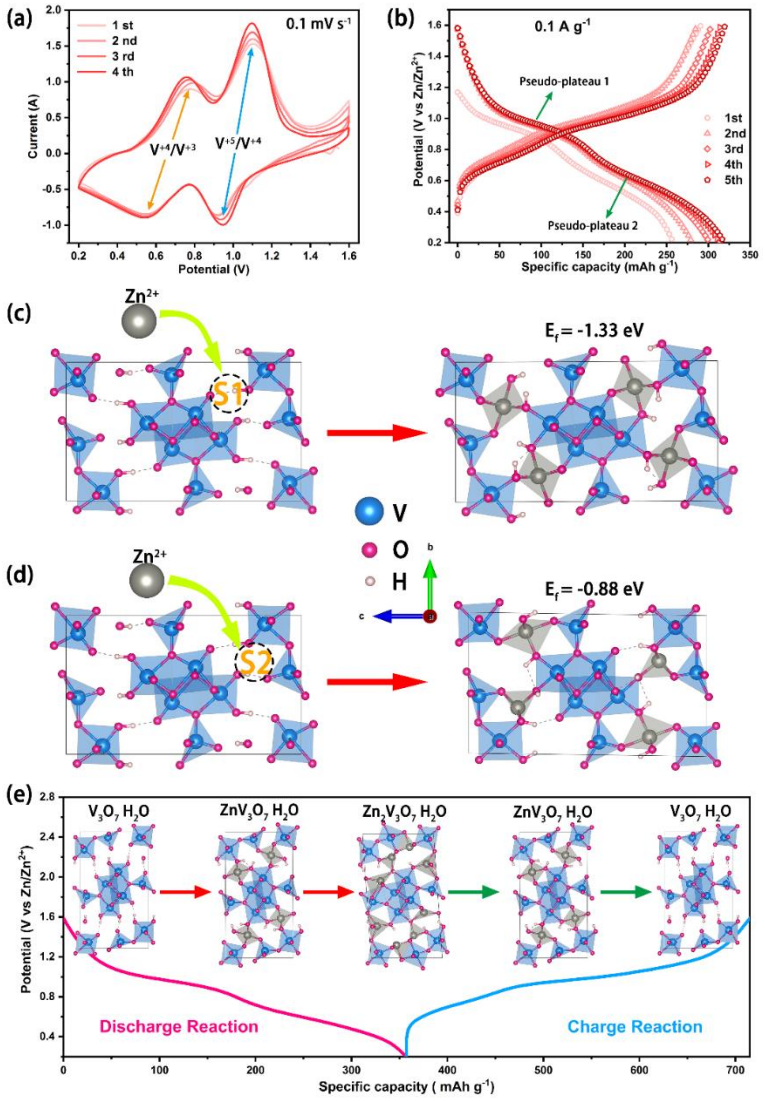

Fig. 4. The two-step Zn ion intercalation in VOHA cathode. (a) The first four cycles of CV curves scanned at 0.1 mV s^{-1}. (b) Galvanostatic charge-discharge profiles at 0.1 A g^{-1}. The insertion

energy of Zn^{2+} into two different host sites of $V_3O_7{\cdot}H_2O$: (c) Site 1 and (d) Site 2. (e) Schematic of the stepwise uptake/extraction process of Zn^{2+} in different discharge/charge depths.

The good performance of the as-prepared ZIB motivated us to further explore the ion de/intercalation mechanism in the $V_3O_7{\cdot}H_2O$ array. As shown in **Fig. 4**a, the as-assembled cell can stably operate in the voltage window of 0.2-1.6 V (*vs* Zn/Zn^{2+}). The CV curves display two pairs of redox peaks, where the peaks located at high potentials (1.1, 0.95 V) are attributed to the transition of $V^{5+} \leftrightarrow V^{4+}$ and the ones at low potentials (0.75, 0.55 V) are ascribed to $V^{4+} \leftrightarrow V^{3+}$. This phenomenon is in good agreement with the charge/discharge profiles in **Fig. 4**b, which show two pairs of pseudo-platforms at 0.95/0.98 and 0.58/0.65 V. It reveals that $V_3O_7{\cdot}H_2O$ might undergo a two-step insertion/extraction of Zn^{2+} in the discharge/charge process. Despite the massive literature about vanadium-based cathodes for ZIBs, few attentions have been paid to the detailed charge-storage mechanism for the $V_3O_7{\cdot}H_2O$ cathode. Herein, we conducted a fundamental investigation by combining theoretical computations and ex-situ analyses to unravel the Zn^{2+} intercalation mechanism.

The Zn ion intercalation is closely related to the crystal structure of cathode materials. As mentioned before, the $V_3O_7{\cdot}H_2O$ has a layered structure, in which the V_3O_8 layers are composed of VO_5 square pyramids and VO_6 octahedra (Fig. 1a, inset). There are mainly two types of active sites for hosting Zn^{2+} between the adjacent V_3O_8 layers, which are denoted as Site 1 and Site 2 (**Fig. 4**c, d). We calculated the formation energy (E_f, eV) of $ZnV_3O_7{\cdot}H_2O$ by Zn^{2+} insertion into the different sites of $V_3O_7{\cdot}H_2O$. The Gibbs free energy of $ZnV_3O_7{\cdot}H_2O$ formation at Site 1 (E_{f1}=-1.33 eV) is smaller than that at Site 2 (E_{f2}=-0.88 eV), therefore the Zn^{2+} would prefer to occupy Site 1, forming $ZnV_3O_7{\cdot}H_2O$ with lower total energy and thus higher stability in the initial discharge stage. In this stage, the vanadium atom with valence state of +5 is reduced to +4 state

accompanied by Zn^{2+} insertion, which is in good agreement with the CV peak and discharge pseudo-platform at the higher voltage. Subsequently, Zn^{2+} would continue to intercalate into Site 2. In this stage, vanadium atoms are further reduced to lower oxidation state (+3) due to the uptake of Zn^{2+}, forming $Zn_2V_3O_7 \cdot H_2O$, which could be the main reason for the second discharge pseudo-plateau. Therefore, the discharge process could be regarded as a two-step intercalation reaction, which can be described as follows:

$$V_3O_7 \cdot H_2O + Zn^{2+} + 2e^- \rightarrow ZnV_3O_7 \cdot H_2O \quad (3)$$

$$ZnV_3O_7 \cdot H_2O + Zn^{2+} + 2e^- \rightarrow Zn_2V_3O_7 \cdot H_2O \quad (4)$$

According to this two-step Zn^{2+} intercalation mechanism, the structural evolution of the cathode material at different discharge/charge depths are illustrated in **Fig. 4**e.

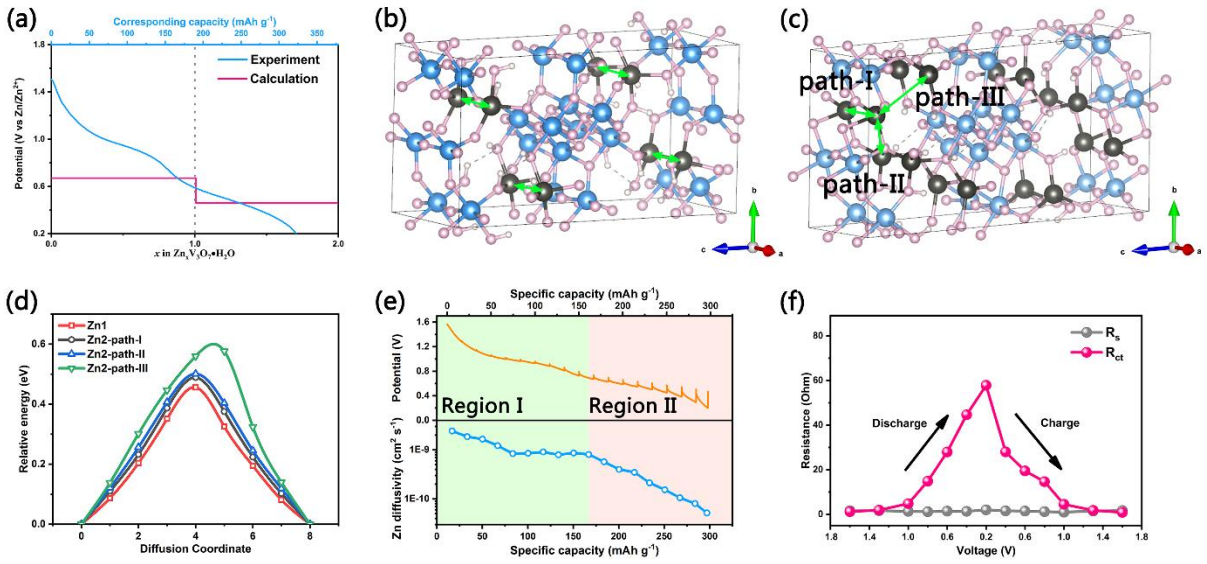

Fig. 5. Electrochemical kinetics analysis of the two-step Zn^{2+} intercalation chemistry. (a) The calculated and experimental discharge curves of the VOHA cathode. (b,c) Diffusion pathways of Zn^{2+} in $ZnV_3O_7 \cdot H_2O$ (b) and $Zn_2V_3O_7 \cdot H_2O$ (c). (d) Diffusion energy barriers for different pathways in (b) and (c). (e) The discharge profile in GITT measurement and corresponding

calculated diffusivity coefficient of Zn^{2+}. (f) The evolution of electrolyte resistance R_s and charge transfer resistance R_{ct} at different discharge/charged states.

The two-step intercalation mechanism was also determined by a thermodynamics calculation based on the density functional theory (DFT). As shown in **Fig. 5**a, the potential of Zn^{2+} insertion is calculated for different discharge depths. Clearly, the potential of $V_3O_7{\cdot}H_2O/ZnV_3O_7{\cdot}H_2O$ reaction is higher than that of $ZnV_3O_7{\cdot}H_2O/Zn_2V_3O_7{\cdot}H_2O$, which is in agreement with the experimental profile of two pseudo-platforms. This proves that the Zn^{2+} is stepwise intercalated into the $V_3O_7{\cdot}H_2O$ crystal, giving arise to the different discharge plateaus. Specifically, the discharge plateau (or peak in CV curve) at higher potential (~0.9 V) originates from the V(+5)→V(+4) reaction, while the lower one (~0.5 V) corresponds to the second electron-transfer reaction of V(+4)→V(+3). Each of these two processes has a theoretical capacity of 189 mAh g^{-1}, thus the total capacity would reach 378 mAh g^{-1} if both reactions can thoroughly proceed. However, it is hard to fully utilize the active materials in practice, owing to the limited migration depth of Zn^{2+}. In this work, the VOHAs cathode with the mass loading 5 mg cm^{-2} exhibits a high material utilization of 85.4% at the current of 0.1 A g^{-1}, owing to the rational design of the microporous nanoarray architecture that allows high electrolyte accessibility and fast ion transport.

The kinetics process of the two-step intercalation behavior was further investigated by DFT calculation and electrochemical analysis. The Zn^{2+} migration paths in the crystal of $ZnV_3O_7{\cdot}H_2O$ and $Zn_2V_3O_7{\cdot}H_2O$ are displayed in **Fig. 5**b-c. In the first stage, Zn ions are mainly accommodated in Sites 1, and diffuse along *a*-axis among the adjacent sites. Then in the subsequent stage, the Zn ions undergo a horizontal diffusion from the initial sites to the neighboring ones, and meanwhile a vertical migration along *a*-axis in $Zn_2V_3O_7{\cdot}H_2O$. Using the nudged elastic band (NEB) method, the Zn diffusion energy barriers for these two cases were evaluated (**Fig. 5**d). The energy barrier

of Zn migration in $ZnV_3O_7 \cdot H_2O$ is 0.456 eV, which is smaller than that of all the three paths in $Zn_2V_3O_7 \cdot H_2O$ (0.488, 0.500 and 0.567 eV for path I, II, and III, respectively), revealing the faster Zn^{2+}-diffusion kinetics in the first intercalation stage. As shown in **Fig. S2**, the discharge platform for the second stage declines more deeply than the first stage when the current rate increases. This implies an inferior electrochemical kinetics for the second Zn^{2+} intercalation step, which is consistent with the DFT analysis [38, 39].

For a quantitative analysis, the zinc diffusion coefficient during the discharge process was estimated from the galvanostatic intermittence titration technique (GITT). The calculated diffusion coefficient (D_{Zn}) of Zn^{2+} in the 5.0-mg cm^{-2} VOHA ranges between 10^{-9} and 10^{-11} cm^2 s^{-1} (**Fig. S3**), which is comparable with most of the reported vanadium-based cathode materials [8,10,27], indicating unimpeded Zn^{2+} diffusion in our high-mass-loading electrode. Interestingly, the Zn^{2+} diffusion coefficient can be also divided into two regions according to different discharge depths, where D_{Zn} values in region I are obviously higher than those in region II (**Fig. 5**e). This corroborates the aforementioned two-step intercalation model. In the initial discharge process, zinc ions preferentially migrate to the vacant Sites 1 in $V_3O_7 \cdot H_2O$ crystalline lattice, which display higher ion diffusivity due to the lower energy barrier. When the Sites 1 are completely occupied, Zn ions subsequently diffuse to the Sites 2. The higher energy barrier for Zn^{2+}-migration and the intensified electrostatic repulsion restrain the Zn^{2+} diffusion, leading to the continuous decline of D_{Zn} in the region II [40-42].

In addition to theoretical calculations, the reaction kinetics of the VOHA cathode were also studied by electrochemical techniques. Electrochemical impedance spectroscopy (EIS) was also employed to investigate the charge transfer kinetics at various charge/discharge stages. The cell was tested at selected potential after reaching a quasi-equilibrium state by holding the voltage for

30 min. The Nyquist plots at various voltages (**Fig. S4**) are composed of a depressed semicircle at high frequencies and a slopping line at low-frequency region, which are described as the charge-transfer resistance (R_{ct}) and the Warburg impedance (Z_w), respectively. The intercept at the real axis reflects the solution resistance (R_s), which is related with the ionic conductivity in the electrolyte. **Fig. 5**f shows the evolution of R_{ct} and R_s in different discharge/charge states [43]. The R_s is very low (< 2 ohm) and keeps constant, indicating the high ionic conductivity at all discharge/charge states. Interestingly, from the fully charged state to the fully discharged state, R_{ct} increases obviously from 1.2 ohm to 57.8 ohm, and the change of R_{ct} is completely reversible in the subsequent charge process. This change of charge-transfer resistance might be ascribed to the reaction kinetics of the electrode interfaces at different discharge/charge depths [44], which is consistent with the evolution of the GITT profiles in **Fig. S3**. In addition, the lines at Warburg region in Nyquist plot are exceptionally inclined within 0.4-1.0 V, which could be interpreted as the remarkable bulk diffusion of the extensive Zn^{2+} in this voltage range [45].

The CV curves at various scan rates were collected to further investigate the electrochemical behaviors of the VOHA-based ZIBs (**Fig. S5**a). The relationship between peak current (i) and corresponding scan rate (v) is demonstrated to obey a power law of $i = av^b$ [46, 47], as shown in **Fig. S5**b, where the b values for the four peaks are determined to be 0.685, 0.718, 0.421 and 0.631, respectively. The small b values, which are close to 0.5, imply the electrode is mainly dominated by the bulk diffusion process. Moreover, the relative electrochemical contribution can be quantitatively calculated via separating the different current responses [48, 49]. For example, the surface-induced capacitive current accounts for 31% of the total contribution at 0.2 mV s^{-1} (**Fig. S5**c). As the sweep rate increases from 0.1 to 1.0 mV s^{-1}, the calculated capacitive contribution stepwise increases from 25% to 58% (**Fig. S5**d). However, the VOHA electrode tends to be

dominated by diffusion-controlled process, which might be related to the enhancive bulk diffusion of Zn^{2+} at high mass loading [50].

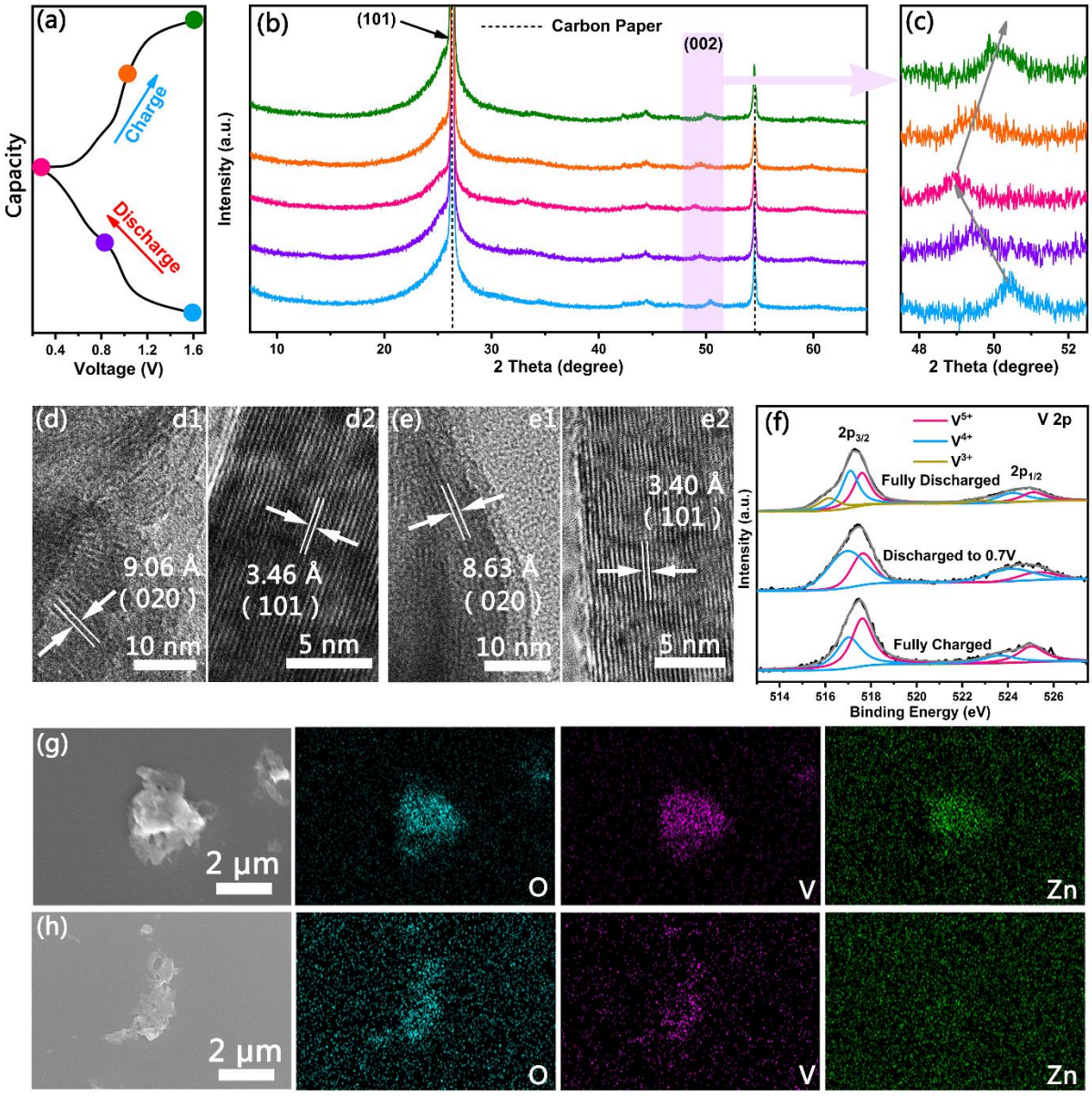

Fig. 6. Ex-situ investigation of the discharge/charge process. (a) The charge/discharge profiles at 0.1 A g^{-1} with a series of selected points to mark the electrode status for subsequent analysis. (b) Ex-situ XRD patterns of VOHA in different selected states and (c) enlarged patterns of the (002) peak of $V_3O_7{\cdot}H_2O$. HRTEM images in fully discharged (d) and charged (e) states. (f) High-resolution XPS spectra of V 2p at fully charged/discharged states together with the one discharged

to 0.7 V. Element mappings of O, V and Zn in discharged (g) and charged (h) states. All samples are prepared from the 5th cycle after rinse with water.

To elucidate the Zn^{2+} de-/intercalation process in depth, a comprehensive study was conducted by combining ex-situ Raman, XRD, TEM, and XPS analyses. The VOHA cathodes in selected discharge/charge states were employed for ex-situ XRD characterizations (**Fig. 6**a). The Raman spectra of the electrodes (**Fig. S6**) at various voltages display no obvious difference, indicating that the crystalline structure of $V_3O_7{\cdot}H_2O$ is well preserved without distortion of the V-O layers even after the deep Zn^{2+} intercalation [51]. In the ex-situ XRD patterns, the characteristic peaks of $V_3O_7{\cdot}H_2O$ remain evident in the whole charge-discharge cycle (**Fig. 6**b), providing an evidence of the reversible structural evolution and a single-phase reaction [52]. In particular, the peak of (002) for $V_3O_7{\cdot}H_2O$ shifts from 50.4° to 49.1° in the discharge process, and returns to its original position in the subsequent charge stage (**Fig. 6**c). The characteristic peak shift toward lower angles indicates the slight expansion of the interlayer spacing during the Zn^{2+} intercalation, and the volume change of the crystal in the Zn^{2+} uptake/extraction process is small enough to avoid structural collapse [51,52]. In addition, the lattice fringes of (020) and (101) planes are observed by the HRTEM (**Fig. 6**d, e), which cannot be detected by XRD due to the weak diffraction signal and the overlap with the substrate signal of carbon paper. The interplanar spacing of (020) varies between 8.63 and 9.06 Å in the charge/discharge process, and the spacing range for (010) crystal plane is between 3.40 and 3.46 Å. The small variation in interlayer spacing is in good agreement with the optimized lattice parameters from DFT calculations (**Fig. S7** and **Table S1**), which show a small expansion of unit-cell volume (~13.1%) for $V_3O_7{\cdot}H_2O$ transforming into $Zn_2V_3O_7{\cdot}H_2O$. The insignificant volume change can avoid the exfoliation of active material during repeated

discharge/charge operation and result in excellent cycle durability, which is especially favorable in the case of large mass loading in the present study [34,53,54].

Finally, the compositional change at charge and discharge states is also evidenced. The high-resolution XPS spectrum (**Fig. 6**f) of VOHA electrode in the fully charged state exhibits a hybrid valence state of V^{4+} and V^{5+} with the domination of the higher oxidation state, corresponding to $V_3O_7{\cdot}H_2O$. The V^{4+} signal becomes stronger and the V^{5+} peak decreases as the electrode is discharged from 1.6 V to 0.7 V. At this state, the $V_3O_7{\cdot}H_2O$ cathode undergoes the first Zn^{2+}-intercalation step with the reaction of $V^{5+}\rightarrow V^{4+}$. When the electrode was further discharged to 0.2 V (fully discharge), a new set of peaks for V^{3+} emerges accompanied with drop of the V^{4+} signal. This is embodiment of the further reduction of vanadium valence due to Zn^{2+} intercalation. Hence, the evolution of XPS spectra provides a direct proof to the proposed two-step Zn^{2+} intercalation chemistry. Finally, the element mappings of discharged VOHA cathode in **Fig. 6**g display a uniform dispersion of Zn element in the fully discharged material (i.e., $Zn_2V_3O_7{\cdot}H_2O$), whereas imperceptible Zn track can be observed in the charged electrode (i.e., $V_3O_7{\cdot}H_2O$), which corroborates the reversible (de)intercalation reaction of Zn^{2+}.

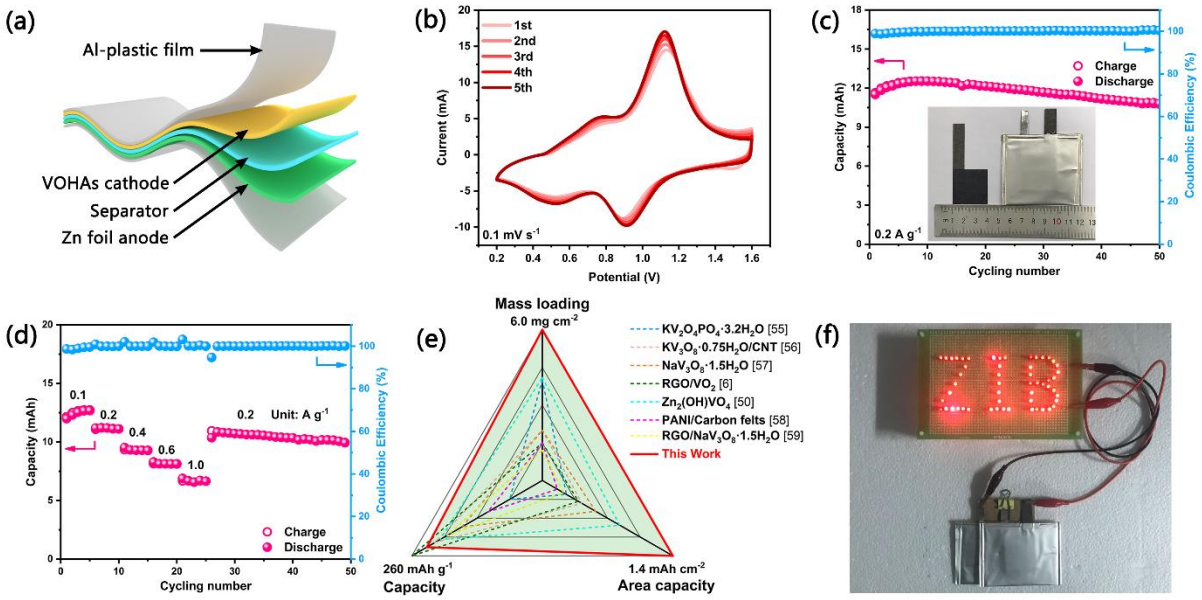

Fig. 7. VOHAs-based pouch cell. (a) Schematic of the pouch cell architecture. (b) CV curves of the first 5 cycles scanned at 0.1 mV s^{-1}. (c) Cycling performance at the specific current of 0.2 A g^{-1}. Inset is the optical photograph of the 3 cm×3 cm cathode and the as-fabricated pouch cell. (d) Rate capability. (e) Performance comparison to reported zinc-ion pouch-type batteries. (f) A LED array (80 mA) powered by two pouch cells in series.

To verify the feasibility in practical application of the self-support VOHAs cathode, prototype pouch batteries were fabricated (**Fig. 7**a). The CV curves with two pairs of redox peaks (**Fig. 7**b) indicate the two-step intercalation mechanism is well reserved in the pouch cells. The pouch cell with 3 cm ×3 cm VOHA cathode delivers a capacity of 11.7 mAh, 92.5% capacity retention after 50 cycles at a low current of 0.2 A g^{-1}. A capacity of 6.7 mAh can be reserved at a high current of 1.0 A g^{-1} (**Fig. 7**c, d). The performance of our pouch cells is comparable or superior to other reported pouch-type batteries based on both gravimetric capacity and areal capacity (**Fig. 7**e) [6,50,55-59]. Two cells in series can power a light-emitting diode (LED) array containing 54 red-light bulbs (**Fig. 7**f). Considering the high performance, safety and low cost, and scalable

fabrication by one-pot synthesis, our free-standing VOHAs could be a promising cathode material for aqueous Zn-ion batteries.

3. Conclusion

We have systematically investigated the Zn-ion intercalation mechanism in $V_3O_7{\cdot}H_2O$ nanoarray through combination of first-principles calculation, electrochemical kinetics analyses, and a series of ex-situ characterizations. The sol-gel based method a facile and green synthesis of high-mass-loading and binder-free VOHA cathode. The empirical model allows one to correlate the mass loading and specific capacity. The optimized mass loading and unique network architecture render high capacity, high-rate capability, and stable cycling of the full aqueous battery. The two-stage Zn^{2+} intercalation has been correlated with the diffusion path, kinetics and associated energy. We propose that the multiple-stage intercalation mechanism established herein might be generic to other high-valence vanadium oxides in their application in Zn or Na ion storage.

4. Experimental Section

4.1 Synthesis of VOHA electrode. To prepare the binder-free $V_3O_7{\cdot}H_2O$ arrays (VOHA) electrode, the carbon paper (CP) was firstly pre-treated in 1.0 M HCl at 120 ℃ for 6 h to serve as the current collector. Then, 0.4 g commercial V_2O_5 powder was mixed with 50 mL 1.0 M HCl aqueous solution and kept stirring overnight to get an amber solution. Subsequently, the CPs were put into the solution and slightly heated at 60 ℃ for 12 h in fuming cupboard. Finally, the VOHA electrode was obtained after the solvent was completely evaporated. To obtain samples with different mass loadings in the range from 1.0 to 12.0 mg cm^{-2}, the volume of reaction solution was changed from 0.2 to 2.0 mL cm^{-2}, accordingly.

4.2 Sample characterization. XRD was conducted by a D/MAX2550 X-ray diffractometer to analyze the phase and crystalline structure of materials. Scanning electron microscopy (SEM, Magellan 400) and transmission electron microscopy (TEM, JEOL JSM-2010F) were employed to investigate morphology characterization. X-Ray photoelectron spectroscopy (XPS) was carried out using a Thermo Escalab 250Xi electron spectrometer.

4.3 Device fabrication and electrochemical measurements. Standard 2032 coin cells were assembled using the VOHA as cathode, Zn plate (Qingyuan Metal Materials Co. Ltd., >99.99%) as anode, glass fiber paper (Whatman GF/D) as separator and aqueous 3 M $Zn(CF_3SO_3)_2$ as electrolyte. The pouch-type batteries were assembled by sandwiching the electrolyte and separator between the 3 cm ×3 cm VOHA cathode and zinc foil, followed by sealing with Al-plastic films. The dosage of electrolyte was about 1.0 mL. The cyclic voltammetry curves and electrochemical impedance spectra (EIS) were collected using a CHI760E electrochemical working station. Galvanostatic cycling studies and galvanostatic intermittent titration technique were conducted by the LAND CT21001A device.

4.4 Computational methods. All calculations were carried out by using the projector augmented wave method in the framework of the density functional theory (DFT) [60], as implemented in the Vienna *ab*-initio Simulation Package (VASP). The generalized gradient approximation (GGA) and Perdew–Burke–Ernzerhof (PBE) exchange functional was used [60]. The plane-wave energy cutoff was set to 500 eV, and the Monkhorst–Pack method was employed for the Brillouin zone sampling [61]. The convergence criterions of energy and force calculations were set to 10^{-5} eV/atom and 0.01 eV $Å^{-1}$, respectively.

During the charging and discharging of an Zn-ion battery, an Zn ion is intercalated or deintercalated from a host crystal structure Zn_xM. For a battery that operates by shuttling nZn^{2+}

ions between the cathode and a pure zinc metal anode, the overall cell reaction can be written as follow [62]: $Zn_{x-n}M$ (s) + nZn (s) = Zn_xM (s), where the typical phase of each compound is indicated for clarity. The forward reaction is the cell discharging reaction, while the reverse is the cell charging reaction. The intercalation potential V (open-circuit) *vs*. Zn/Zn^{2+} can then be calculated using the following expression [63]:

$$V = -[\mathrm{E}(\mathrm{Zn}_{x1}\mathrm{M}) - \mathrm{E}(\mathrm{Zn}_{x2}\mathrm{M}) - (x_1 - x_2)\mathrm{E}(\mathrm{Zn})] \Big/ (x_1 - x_2)2\mathrm{e} \qquad (5)$$

where E is the total electronic energy (in eV) from DFT calculations, e is the absolute value of the electron charge, and x_1 and x_2 are the numbers of Zn atoms contained in the intercalated and deintercalated host materials, respectively. Here, the zero-point energy differences, thermal phonon energies, and entropic effects are reasonably neglected, since the vibrational and configurational entropy contributions to the cell voltage at room temperature is expected to be small [62,64]. The energy barriers for Zn ion diffusion in $V_3O_7{\cdot}H_2O$ were calculated by the nudged elastic band (NEB) method and the 3×1×1 supercell model [65].

4.5 Galvanostatic intermittence titration technique (GITT). The diffusion coefficient (D_{Zn}) was determined according to the following equation [40,41]:

$$D = \frac{4L^2}{\pi\tau}\left(\frac{\Delta E_s}{\Delta E_t}\right)^2 \qquad (6)$$

where τ refers to duration time (s) of the current pulse, L represents the Zn^{2+} diffusion length (cm, that is equal to the thickness of active material), ΔE_s corresponds to the steady-state potential change (V) caused by the current pulse, and ΔE_t is the direct change of voltage (V) before relaxation. In this measurement, current pulse of 0.1 A g^{-1} was applied for 600 s and the relaxation time was 1800 s.

Acknowledgements

H.J. F. acknowledges the financial support from Ministry of Education by Tier 1 grant (RG10/18). The authors acknowledge financial support from National Natural Science Foundation of China (NSFC Grant No. 21571080).

References

[1] D. Chao, W. Zhou, F. Xie, C. Ye, H. Li, M. Jaroniec, S.-Z. Qiao, Sci. Adv. 6 (2020) eaba4098.
[2] J.F. Parker, C.N. Chervin, I.R. Pala, M. Machler, M.F. Burz, J.W. Long, D.R. Rolison, Science 356 (2017) 415-418.
[3] D. Kundu, B.D. Adams, V. Duffort, S.H. Vajargah, L.F. Nazar, Nat. Energy 1 (2016) 16119.
[4] H. Li, C. Han, Y. Huang, Y. Huang, M. Zhu, Z. Pei, Q. Xue, Z. Wang, Z. Liu, Z. Tang, Y. Wang, F. Kang, B. Li, C. Zhi, Energy Environ. Sci. 11 (2018) 941-951.
[5] W. Wang, V.S. Kale, Z. Cao, S. Kandambeth, W. Zhang, J. Ming, P.T. Parvatkar, E. Abou-Hamad, O. Shekhah, L. Cavallo, M. Eddaoudi, H.N. Alshareef, ACS Energy Lett. 5 (2020) 2256-2264.
[6] X. Dai, F. Wan, L. Zhang, H. Cao, Z. Niu, Energy Storage Mater. 17 (2019) 143-150.
[7] Y. Huang, J. Zhang, J. Liu, Z. Li, S. Jin, Z. Li, S. Zhang, H. Zhou, Mater. Today Energy 14 (2019) 100349.
[8] J. Ding, Z. Du, B. Li, L. Wang, S. Wang, Y. Gong, S. Yang, Adv. Mater. 31 (2019) e1904369.
[9] M. Song, H. Tan, D. Chao, H.J. Fan, Adv. Funct. Mater. 28 (2018) 1802564.
[10] C. Wu, H. Tan, W. Huang, C. Liu, W. Wei, L. Chen, Q. Yan, Mater. Today Energy 19 (2021) 100595.
[11] H. Luo, B. Wang, F. Wu, J. Jian, K. Yang, F. Jin, B. Cong, Y. Ning, Y. Zhou, D. Wang, H. Liu, S. Dou, Nano Energy 81 (2021) 105601.
[12] D. Chen, M. Lu, B. Wang, R. Chai, L. Li, D. Cai, H. Yang, B. Liu, Y. Zhang, W. Han, Energy Storage Mater. 35 (2021) 679-686.
[13] X. Jia, C. Liu, Z.G. Neale, J. Yang, G. Cao, Chem. Rev. 120 (2020) 7795-7866.
[14] N. Liu, X. Wu, L. Fan, S. Gong, Z. Guo, A. Chen, C. Zhao, Y. Mao, N. Zhang, K. Sun, Adv. Mater. 32 (2020) e1908420.
[15] T. Xue, H.J. Fan, J. Energy Chem. 54 (2021) 194-201.
[16] L.E. Blanc, D. Kundu, L.F. Nazar, Joule 4 (2020) 771-799.
[17] J. Ding, Z. Du, L. Gu, B. Li, L. Wang, S. Wang, Y. Gong, S. Yang, Adv. Mater. 30 (2018) e1800762.
[18] B.Y. Tang, L.T. Shan, S.Q. Liang, J. Zhou, Energy Environ. Sci., 12 (2019) 3288-3304.
[19] D. Selvakumaran, A. Pan, S. Liang, G. Cao, J. Mater. Chem. A 7 (2019) 18209-18236.
[20] L. Ma, S. Chen, C. Long, X. Li, Y. Zhao, Z. Liu, Z. Huang, B. Dong, J.A. Zapien, C. Zhi, Adv. Energy Mater. 9 (2019) 1902446.
[21] D. Chen, M. Lu, D. Cai, H. Yang, W. Han, J. Energy Chem. 54 (2021) 712-726.
[22] K.W. Nam, H. Kim, Y. Beldjoudi, T.W. Kwon, D.J. Kim, J.F. Stoddart, J. Am. Chem. Soc. 142 (2020) 2541-2548.
[23] Q. Zhao, W. Huang, Z. Luo, L. Liu, Y. Lu, Y. Li, L. Li, J. Hu, H. Ma, J. Chen, Sci. Adv. 4 (2018) eaao1761.
[24] F. Wan, Z. Niu, Angew. Chem. Int. Ed. 58 (2019) 16358-16367.
[25] X. Wang, L. Ye, Y. Zou, L. Zhao, Q. Jiang, Mater. Today Energy 19 (2021) 100593.

[26] X. Li, L. Ma, Y. Zhao, Q. Yang, D. Wang, Z. Huang, G. Liang, F. Mo, Z. Liu, C. Zhi, Mater. Today Energy 14 (2019) 100361.
[27] P. He, Y. Quan, X. Xu, M. Yan, W. Yang, Q. An, L. He, L. Mai, Small, 13 (2017) 1702551.
[28] Z. Cao, H. Chu, H. Zhang, Y. Ge, R. Clemente, P. Dong, L. Wang, J. Shen, M. Ye, P.M. Ajayan, J. Mater. Chem. A 7 (2019) 25262-25267.
[29] Q. Pang, C. Sun, Y. Yu, K. Zhao, Z. Zhang, P.M. Voyles, G. Chen, Y. Wei, X. Wang, Adv. Energy Mater. 8 (2018) 1800144.
[30] M. Rastgoo-Deylami, M.S. Chae, S.-T. Hong, Chem. Mater. 30 (2018) 7464-7472.
[31] C. Zhang, H. Song, C. Zhang, C. Liu, Y. Liu, G. Cao, J. Phy. Chem. C 119 (2015) 11391-11399.
[32] W. Duan, M. Zhao, Y. Li, N.u.R. Lashari, T. Xu, F. Wang, X. Song, Energy & Fuels 34 (2020) 3877-3886.
[33] Q. Yang, Y. Guo, B. Yan, C. Wang, Z. Liu, Z. Huang, Y. Wang, Y. Li, H. Li, L. Song, J. Fan, C. Zhi, Adv. Mater. 32 (2020) e2001755.
[34] W. Zhou, D. Zhu, J. He, J. Li, H. Chen, Y. Chen, D. Chao, Energy Environ. Sci. 13 (2020) 4157-4167.
[35] S.-H. Lee, H.M. Cheong, M.J. Seong, P. Liu, C.E. Tracy, A. Mascarenhas, J.R. Pitts, S.K. Deb, Solid State Ionics 165 (2003) 111-116.
[36] S. Petnikota, J.J. Toh, J.Y. Li, R. Chua, M. Srinivasan, ChemElectroChem 6 (2019) 493-503.
[37] R. Li, C.-Y. Liu, Mater. Res. Bull. 45 (2010) 688-692.
[38] K. Zhu, T. Wu, K. Huang, ACS Nano 13 (2019) 14447-14458.
[39] D. Kundu, S. Hosseini Vajargah, L. Wan, B. Adams, D. Prendergast, L.F. Nazar, Energy Environ. Sci. 11 (2018) 881-892.
[40] Y. Yang, Y. Tang, G. Fang, L. Shan, J. Guo, W. Zhang, C. Wang, L. Wang, J. Zhou, S. Liang, Energy Environ. Sci. 11 (2018) 3157-3162.
[41] L. Xu, Y. Zhang, J. Zheng, H. Jiang, T. Hu, C. Meng, Mater. Today Energy 18 (2020) 100509.
[42] Y. Liu, Q. Li, K. Ma, G. Yang, C. Wang, ACS Nano 13 (2019) 12081-12089.
[43] K. Zhu, T. Wu, S. Sun, W. van den Bergh, M. Stefik, K. Huang, Energy Storage Mater. 29 (2020) 60-70.
[44] G.Z. Fang, Z.X. Wu, J. Zhou, C.Y. Zhu, X.X. Cao, T.Q. Lin, Y.M. Chen, C. Wang, A.Q. Pan, S.Q. Liang, Adv. Energy Mater. 8 (2018) 1703155.
[45] M. Zarrabeitia, F. Nobili, M.Á. Muñoz-Márquez, T. Rojo, M. Casas-Cabanas, J. Power Sources 330 (2016) 78-83.
[46] N. Zhang, Y. Dong, M. Jia, X. Bian, Y. Wang, M. Qiu, J. Xu, Y. Liu, L. Jiao, F. Cheng, ACS Energy Lett. 3 (2018) 1366-1372.
[47] H. Luo, B. Wang, C. Wang, F. Wu, F. Jin, B. Cong, Y. Ning, Y. Zhou, D. Wang, H. Liu, S. Dou, Energy Storage Mater. 33 (2020) 390-398.
[48] D. Chen, M. Lu, L. Li, D. Cai, J. Li, J. Cao, W. Han, J. Mater. Chem. A 7 (2019) 21759-21765.
[49] H. Luo, B. Wang, F. Wang, J. Yang, F. Wu, Y. Ning, Y. Zhou, D. Wang, H. Liu, S. Dou, ACS Nano 14 (2020) 7328-7337.
[50] D. Chao, C.R. Zhu, M. Song, P. Liang, X. Zhang, N.H. Tiep, H. Zhao, J. Wang, R. Wang, H. Zhang, H.J. Fan, Adv. Mater. 30 (2018) e1803181.
[51] S. Liu, H. Zhu, B. Zhang, G. Li, H. Zhu, Y. Ren, H. Geng, Y. Yang, Q. Liu, C.C. Li, Adv. Mater. 32 (2020) e2001113.

[52] L. Chen, Y. Ruan, G. Zhang, Q. Wei, Y. Jiang, T. Xiong, P. He, W. Yang, M. Yan, Q. An, L. Mai, Chem. Mater. 31 (2019) 699-706.
[53] Z. Wu, C. Lu, Y. Wang, L. Zhang, L. Jiang, W. Tian, C. Cai, Q. Gu, Z. Sun, L. Hu, Small 16 (2020) e2000698.
[54] L. Wang, K.-W. Huang, J. Chen, J. Zheng, Sci. Adv. 5 (2019) eaax4279.
[55] X. Yang, W. Deng, M. Chen, Y. Wang, C.F. Sun, Adv. Mater. 32 (2020) e2003592.
[56] F. Wan, S. Huang, H. Cao, Z. Niu, ACS Nano 14 (2020) 6752-6760.
[57] F. Wan, L. Zhang, X. Dai, X. Wang, Z. Niu, J. Chen, Nat. Commun. 9 (2018) 1656.
[58] F. Wan, L. Zhang, X. Wang, S. Bi, Z. Niu, J. Chen, Adv. Funct. Mater. 28 (2018) 1804975.
[59] F. Wan, X. Wang, S. Bi, Z. Niu, J. Chen, Sci. China Chem. 62 (2019) 609-615.
[60] W. Kohn, L. J. Sham, Phys. Rev. 140 (1965) A1133-A1138.
[61] H. J. Monkhorst, J. D. Pack, Phys. Rev. B 13 (1976) 5188-5192.
[62] S. P. Ong, V. L. Chevrier, G. Hautier, A. Jain, C. Moore, S. Kim, X. Ma, G. Ceder, Energy Environ. Sci. 4 (2011) 3680-3688.
[63] A. Urban, D.-H. Seo, G. Ceder, npj Comput. Mater. 2 (2016) 16002.
[64] M. S. Islam, C. A. Fisher, Chem. Soc. Rev. 43 (2014) 185-204.
[65] G. Henkelman, B. P. Uberuaga, H. Jónsson, J. Chem. Phys. 113 (2000) 9901.